Supporting Information

An Ultrasmall Ordered High-Entropy Intermetallic with Multiple Active Sites for the Oxygen Reduction Reaction

Tao Chen, †[a] Chunyu Qiu, †[b] Xinkai Zhang, †[c] Hangchao Wang, †[a] Jin Song,[a] Kun Zhang,[a] Tonghuan Yang,[a] Yuxuan Zuo,[a] Yali Yang,[a] Chuan Gao,[a] Wukun Xiao,[a] Zewen Jiang,[a] Yucheng Wang,[b] Yan Xiang,[c] Dingguo Xia,*[a]

AUTHOR ADDRESS:

[a] Beijing Key Laboratory of Theory and Technology for Advanced Batteries Materials, School of Materials Science and Engineering, Peking University, Beijing 100871, PR China.

[b] State Key Laboratory of Physical Chemistry of Solid Surfaces, Collaborative innovation center of Chemistry for Energy Materials, College of Chemistry and Chemical Engineering, Xiamen University, Xiamen, 361005, China.

[c] Beijing Key Laboratory of Bio-inspired Energy Materials and Devices, School of Space and Environment, Beihang University, Beijing, 100191, China

† Contribute equally to this work.

Method Details

Synthesis of Zn-DPCN: Typically, 1.118 g zinc (II) nitrate hexahydrate (Beijing Tongguang fine chemical Company, AR) was dissolved in a methanol (Sigma-Aldrich, AR) solution and the other methanol solution contained 1.232 g 2-methylimidazole (Sigma-Aldrich, AR). After 30 min of magnetic stirring, mixed the two solutions and continuous stirred at room temperature for 24 hours. Then the precipitate was collected by centrifugation, washed at least three times with methanol, then dried at 70°C in a vacuum oven for 10 hours. The precursors are designated as ZIF-8, subsequently ZIF-8 were heated at a temperature of 900 °C in a tube furnace under Ar/H_2 flow for 3 hours to obtain the Zn-DPCN, and then the products were treated in 0.5 M H_2SO_4 for 1h to remove partially unstable zinc. Subsequently washed until PH is neutral, collected by centrifugation and dried, the pretreated Zn-DPCN support can be obtained.

Synthesis of PFCNCZ-HEI: In detail, the corresponding proportion of $Co(acac)_2$, (Sigma-Aldrich, AR) ($Fe(acac)_3$), (Sigma-Aldrich, AR) ($Ni(acac)_2$), (Sigma-Aldrich, AR) ($Cu(acac)_2$) (Sigma-Aldrich, AR) and $H_2PtCl_6{\cdot}6H_2O$ (Sigma-Aldrich, AR) were first dissolved in 20 mL mixture of water and alcohol. Among them, the input amount of each non-precious metal was 0.005mMol, and the addition amount of $H_2PtCl_6{\cdot}6H_2O$ at 10mM concentration was 0.6mL. Then, 25 mg Zn-DPCN support was dispersed in the solution and ultrasound for half an hour. The suspension was heated at 70 ℃ with magnetic stirring to evaporate solvent. The obtained thick slurry was then transferred into an oven to dry overnight to guarantee a completely drying. After grounding in an agate mortar, the powder was annealed and alloyed at 800 ℃ for four hours under flowing H_2/Ar. After treatment with 0.1M $HClO_4$ solution for half an hour, centrifuge and dry overnight. The as-prepared reference samples with different atomic ratios were synthesized in the same procedure. The reference samples of different synthetic temperatures and different loads are also synthesized in the same procedure but except for changing the final calcination temperature and metal precursor respectively. PFCNCZ-HEA was synthesized under identical conditions except for a modification in the synthesis temperature to 600°C. The synthesis of binary intermetallic reference samples was also conducted under the same conditions, with the exception of incorporating only two types of metal ions.

Characterization: XRD patterns were recorded on a Bruker D8 Focus XRD at a scan rate of 1° min^{-1} with Cu K radiation. TEM test was carried out using a JEOL 2010F microscope operated at 200 kV. The high-resolution STEM images, STEM-EDX mapping, and line-scan were carried out under a Cs-corrected STEM (FEI Titan Themis Z) operated at 300 kV with a convergence semi-angle of 25 mrad, which was corrected by probe SCOR spherical aberration corrector. ICP-AES was measured on a Prodigy 7 ICP-AES. The sample was pressed into a block for performing the XRF analysis. XPS was performed using a VG ESCALAB MKII instrument, which uses Mg Kα X-ray source. The Fe, Co, Ni, Cu and Zn K-edge spectra and Pt L_3-edge were collected at in the fluorescence mode at beamline 1W2B with a Si (111) double-crystal monochromator at the Beijing Synchrotron Radiation Facility (BSRF). ATHENA software package was used to analyse the XANES and extended X-ray absorption fine-structure data. [1] Synchrotron XRD measurements were performed at the Shanghai Synchrotron Radiation Facility with a high energy (18keV, λ=0.686 Å).

Electrochemical Measurements: Electrochemical experiments were tested in a three-electrode cell using a CHI 760E. Glassy carbon rotating disk electrode was served as the working electrode. A $Hg/HgSO_4$ electrode was used as the reference electrode, and Pt wire were used as the counter electrode. 2mg carbon-supported catalyst was dispersed in the mixture of 490 μL isopropanol, 490 μL deionized water and 20 μL Nafion (5%). The mixture was sonicated for 30 min to obtain a homogeneous catalyst ink. Finally, 2 μL catalyst ink cast onto glassy carbon rotating disk electrode with 4mm diameter and dry naturally. CV curves were conducted in N_2-saturated 0.1 M $HClO_4$ with a sweep rate 50 mV s^{-1}. The ORR polarization curves were tested in O_2-saturated 0.1 M $HClO_4$ at a scanning rate of 10 mV s^{-1} with iR drop correction. The

accelerated durability test (ADT) was performed at by potential sweeps between 0.6 and 1.1 V for 10000 cycles with 100 mV s^{-1}.

Computational details: All the density functional theory (DFT) calculations were carried out with the Vienna ab initio simulation package (VASP)[1] code. To represent the electron−ion interactions, the Projector augmented wave (PAW) potentials were employed, and the Perdew−Burke−Ernzerhof (PBE) functional within the generalized gradient approximation (GGA) was adopted to describe the electron exchange-correlationinteractions[2-4]. The cutoff energy was set to 500 eV, and the convergence criteria for energy and force were 10-5 eV and 0.02 eV/Å, respectively. During slab models construction, 15 Å vacuum space was adopted to reduce the influence of adjacent images. For all the calculations of slab models, a K-spacing value of 0.08 was used to generate K-Mesh. The dispersion-corrected DFT-D3 method was used to describe the van der Waals (vdW) interactions[5].

Single fuel cell preparation and test: Catalyst ink for 30% nafion electrodes was made by ultrasonically mixing the catalyst, deionized water, isopropanol, and 5wt% Nafion ionomer solution for 1h. Then the catalyst slurry was applied to the carbon paper by spraying to form the cathode catalyst layer with loading of 0.03 mg_{Pt} cm^{-2}. As for anode, Pt/C (20 wt. % of Pt, JM Hispec3000) was used with loading of 0.1 mg_{Pt} cm^{-2}. The prepared cathode and anode were pressed onto the two sides of a Nafion 211 membrane (DuPont) at 120 °C to obtain the membrane electrode assembly. The geometric area of the MEA was 12.25 cm^2. The fuel cell performance was measured with 850e Fuel Cell Test Station. The gases were humidified at 80 °C with the flow rate of 0.6 L min^{-1} for H_2 and 2.6 L min^{-1} for O_2. The absolute pressure was 1.0 bar for H_2 and 0.5-2 bar for O_2.

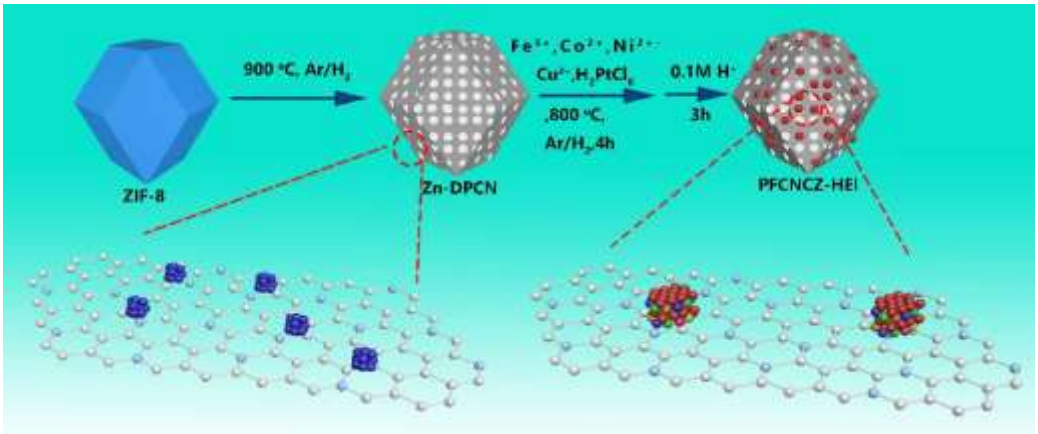

Figure S1. Simplified schematic diagram of PFCNCZ-HEI preparation.

Table S1. ICP-AES of Zn-DPCN.

sample	element	Content (wt%)
Zn-DPCN	Zn	4.32

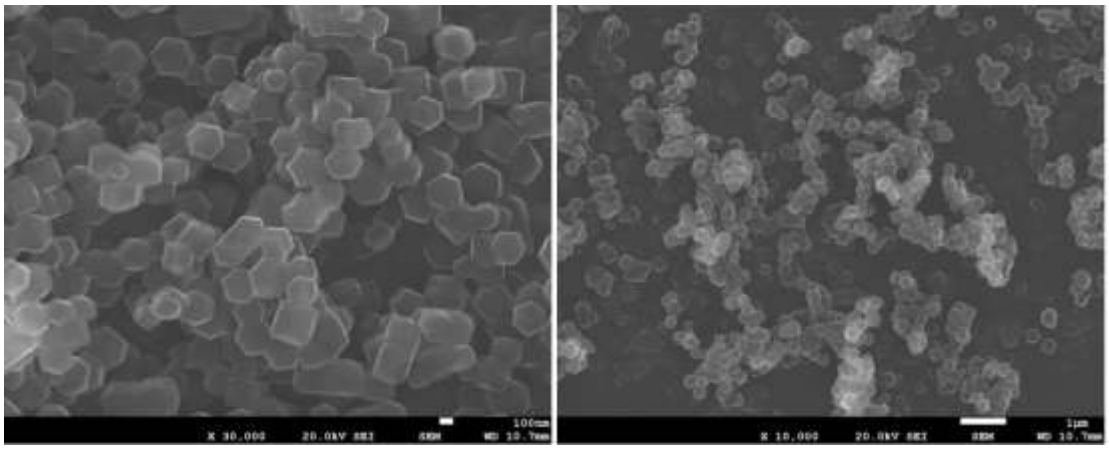

Figure S2. SEM images of ZIF-8.

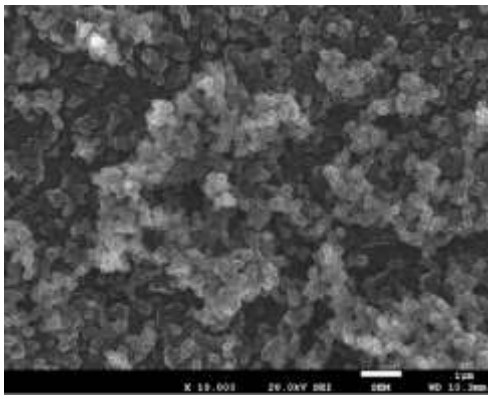

Figure S3. SEM images of Zn-DPCN.

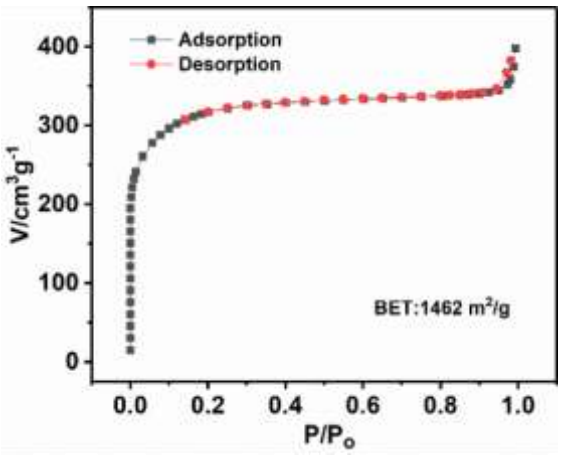

Figure S4. N_2 adsorption–desorption isotherms of Zn-DPCN.

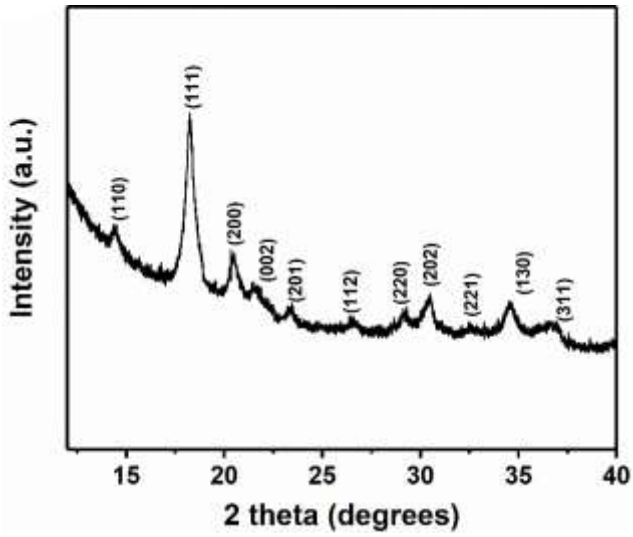

Figure S5. Synchrotron XRD patterns of the PFCNCZ-HEI nanoparticles. Synchrotron XRD measurements were performed at the Shanghai Synchrotron Radiation Facility with a high energy (18keV, λ=0.686 Å).

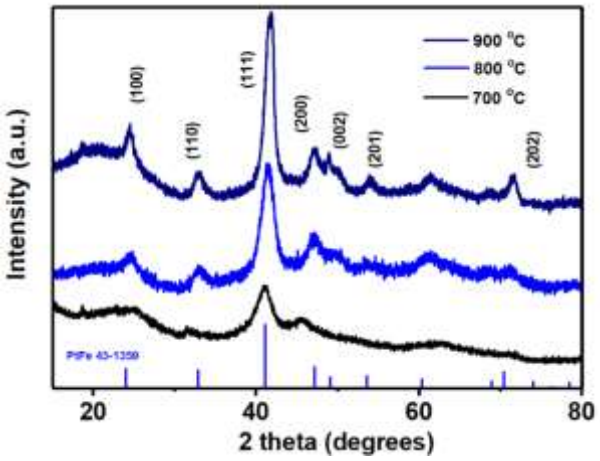

Figure S6. XRD patterns of PFCNCZ-HEI synthesized at different temperatures.

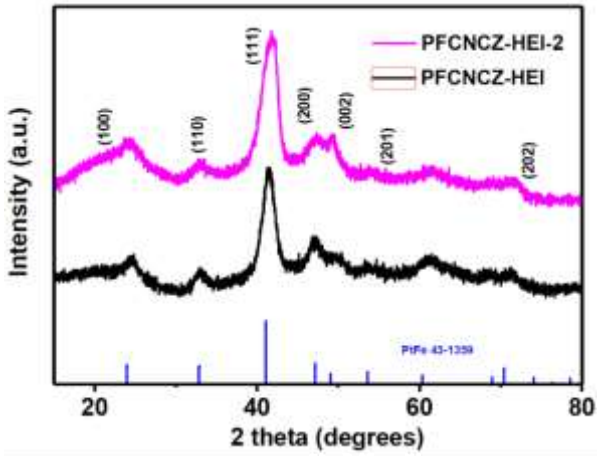

Figure S7. XRD patterns of PFCNCZ-HEI with different contents. (The mass load of each metal element of PFCNCZ-HEI-2 is twice that of PFCNCZ-HEI)

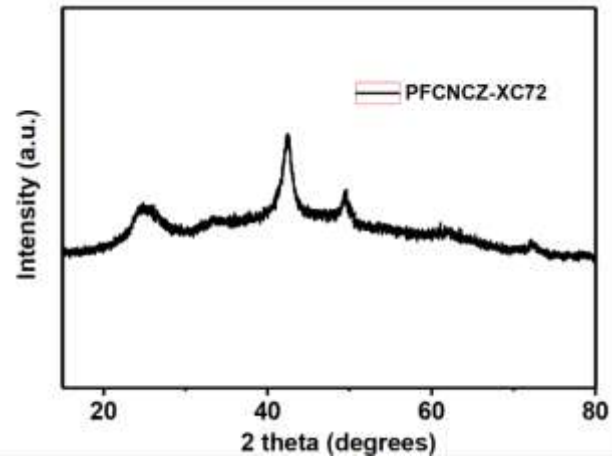

Figure S8. XRD patterns of PFCNCZ-XC72 prepared with XC72 as carbon support.

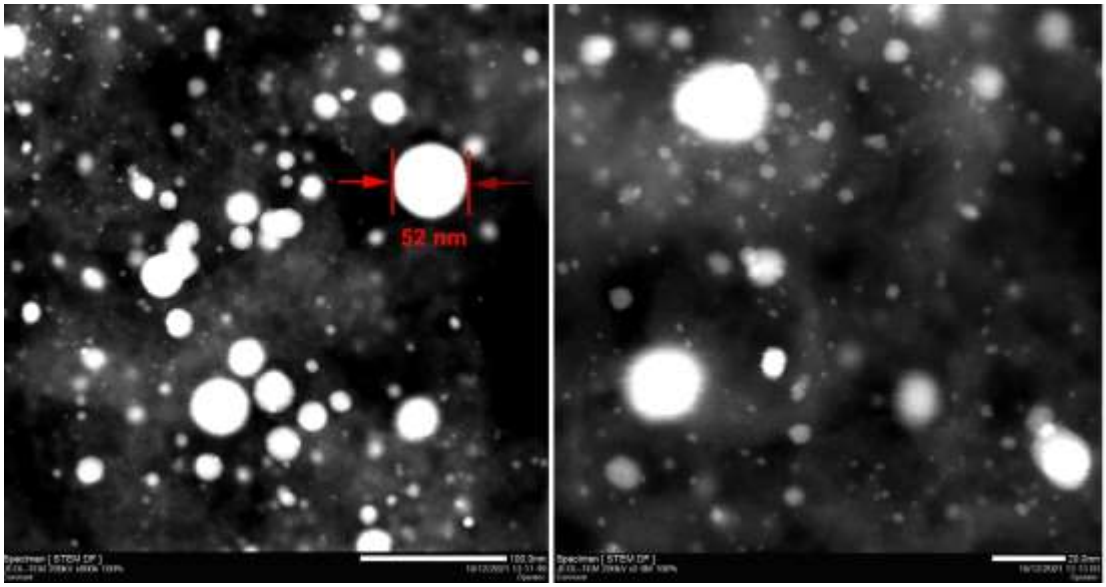

Figure S9. TEM images of PFNCZ-XC72 reference sample.

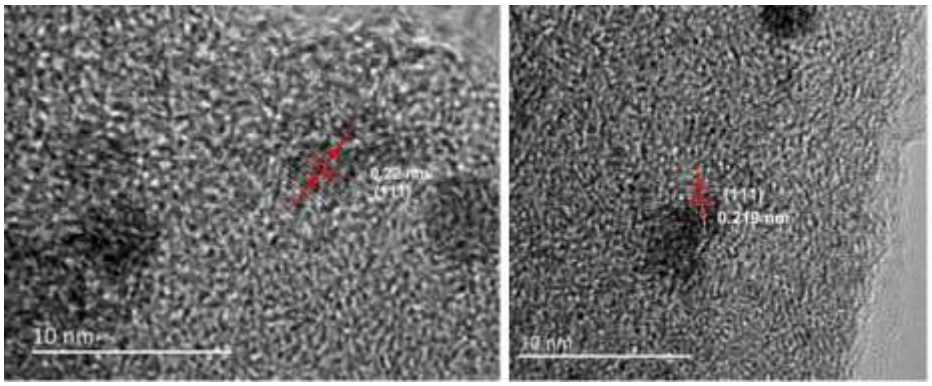

Figure S10. TEM images of PFCNCZ-HEI nanoparticles.

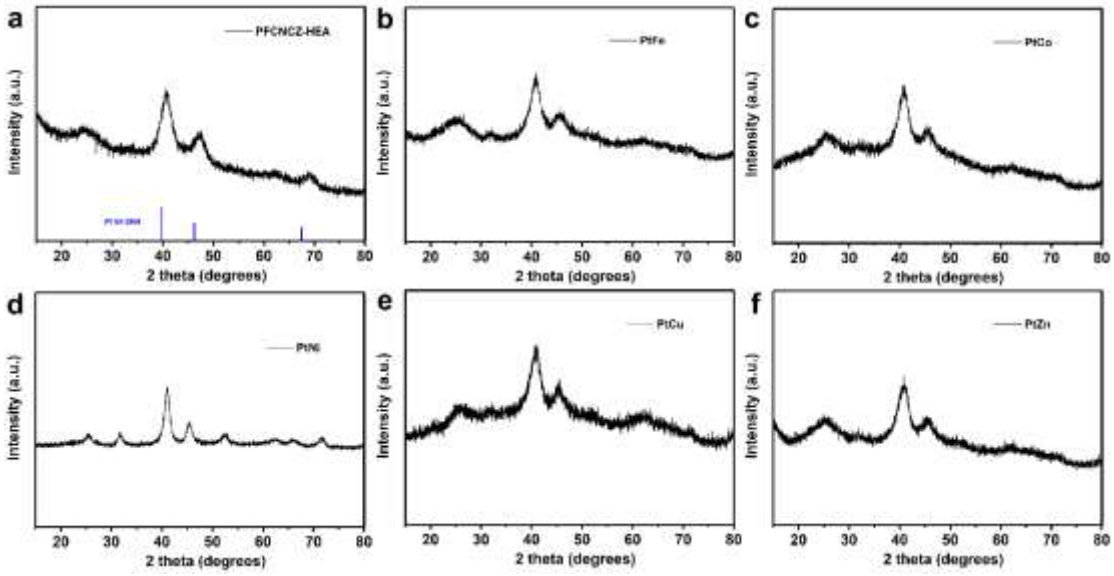

Figure S11. (a) XRD patterns of PFCNCZ-HEA reference sample prepared at 600 ºC; XRD patterns of (b) PtFe, (c) PtCo, (d) PtNi, (e) PtCu and (f) PtZn binary intermetallic reference sample synthesized under identical conditions.

As shown in Figure S11a, the PFCNCZ-HEA corresponds to the peak of the Pt solid solution alloy. The shift of the diffraction peak towards higher angles is indicative of the alloying of Pt with multiple elements. Additionally, distinct intermetallic characteristic crystal planes, specifically the (110) planes located around 31.8°, can be observed in the XRD diffraction peaks of PtFe, PtCo, PtNi, PtCu, and PtZn (successively corresponding to figures S11b-f.)

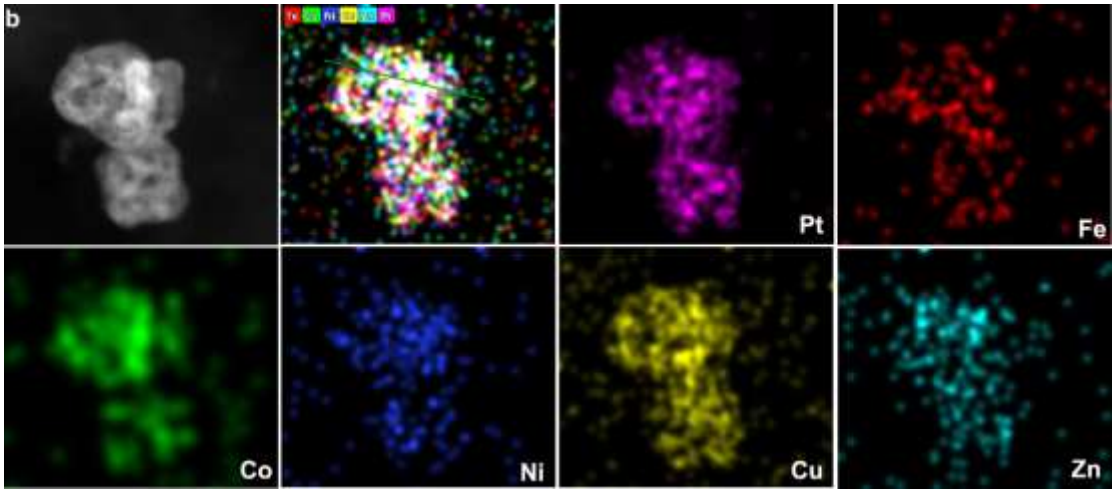

Figure S12. (a-c) STEM-EDS mapping of different PFCNCZ-HEI nanoparticles.

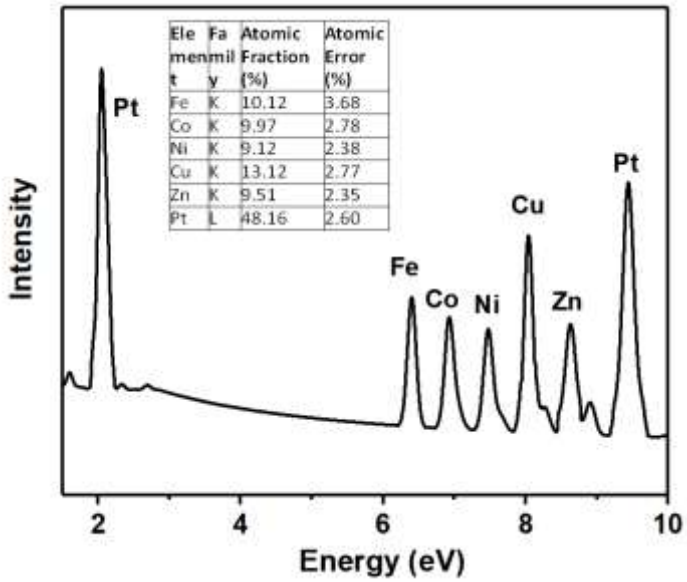

Figure S13. EDS spectrum of the as-prepared PFCNCZ-HEI nanoparticles.

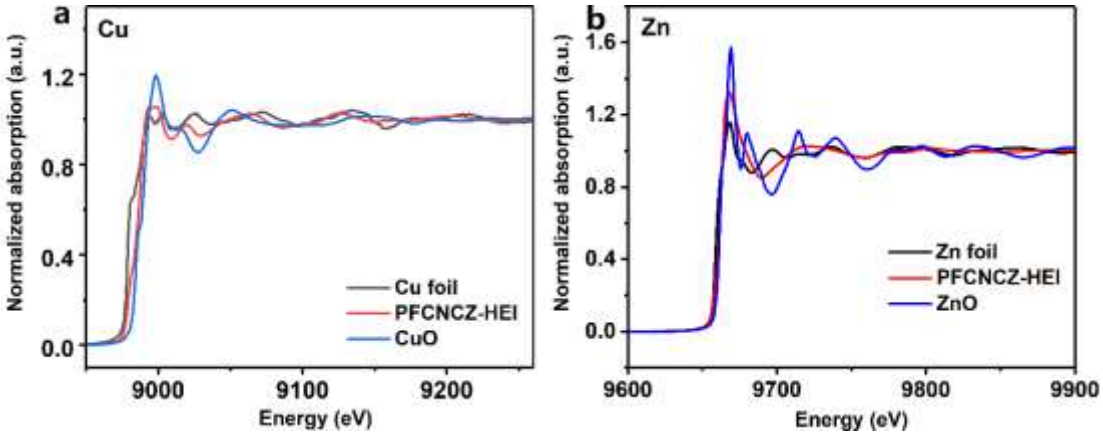

Figure S14. K-edge XANES spectra of (a) Cu and (b) Zn in PFCNCZ-HEI nanoparticles.

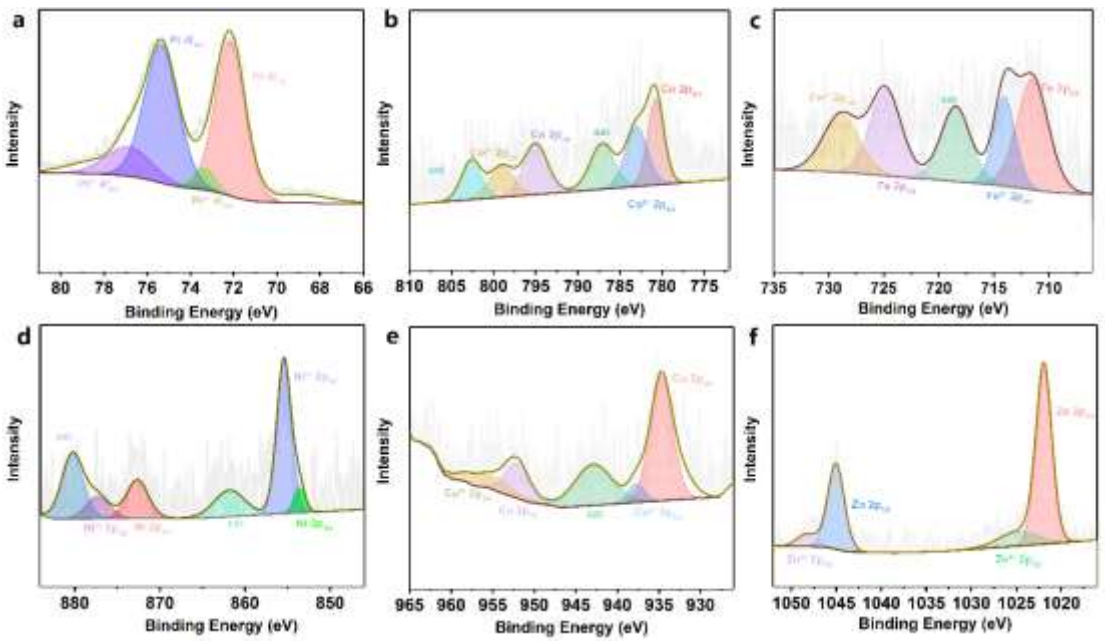

Figure S15. XPS spectra collected at the (a) Pt 4f, (b) Co 2p, (c) Fe2p, (d) Ni 2p, (e) Cu 2p, (f) Zn 2p edges for the PFCNCZ-HEI nanoparticles.

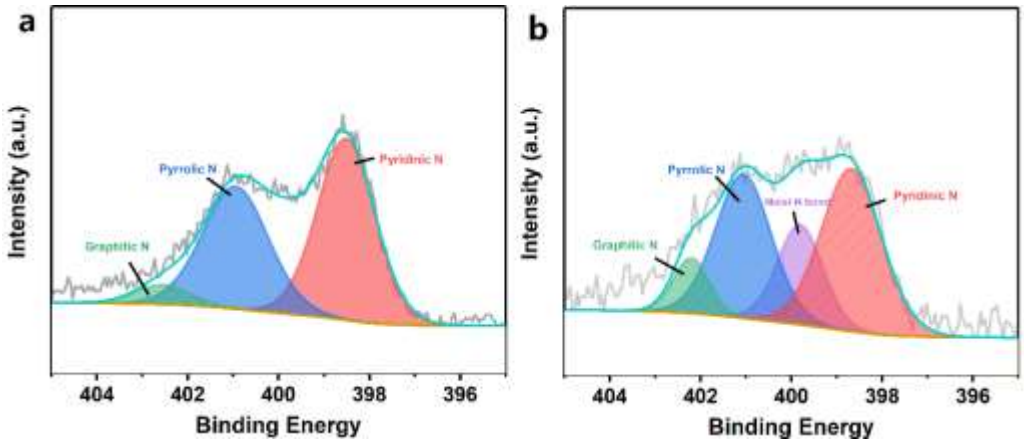

Figure S16. XPS spectra collected at the N 1s edges for the (a) Zn-DPCN and (b) PFCNCZ-HEI samples.

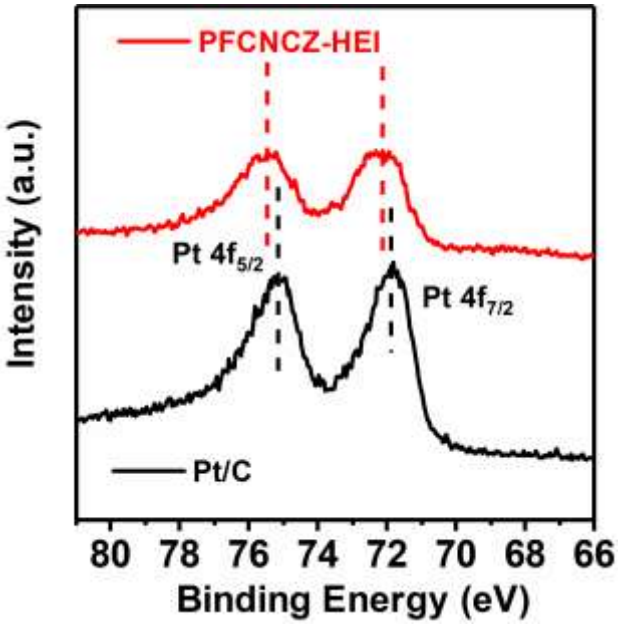

Figure S17. XPS spectra at Pt 4f for PFCNCZ-HEI sample and Pt/C reference.

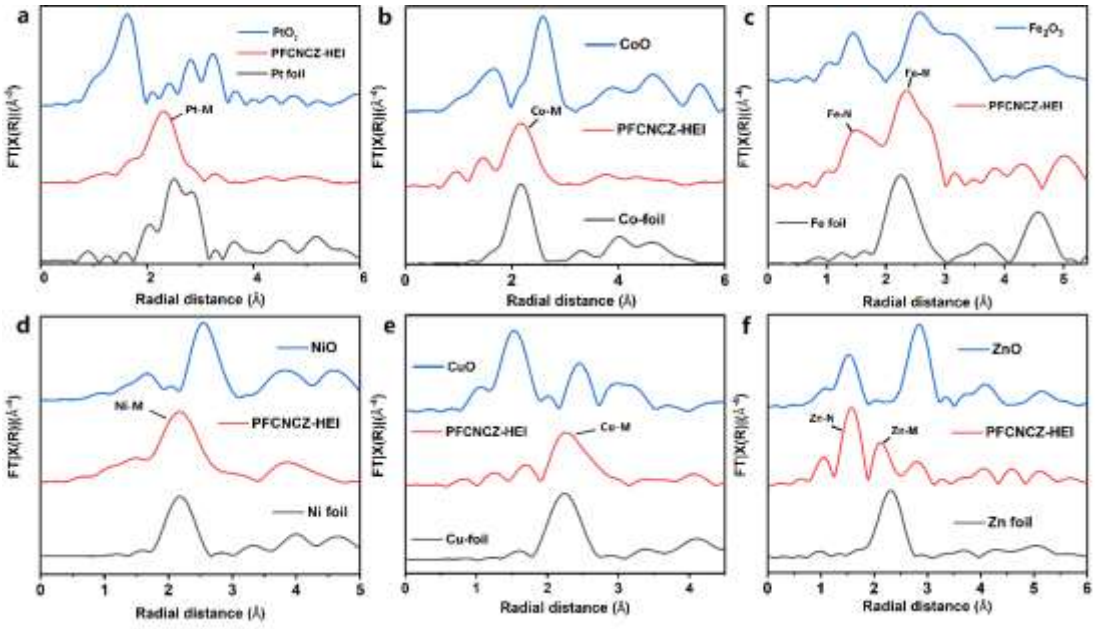

Figure S18. FT-EXAFS spectra of (a) Pt, (b) Co, (c) Fe, (d) Ni, (e) Cu, and (f) Zn elements.

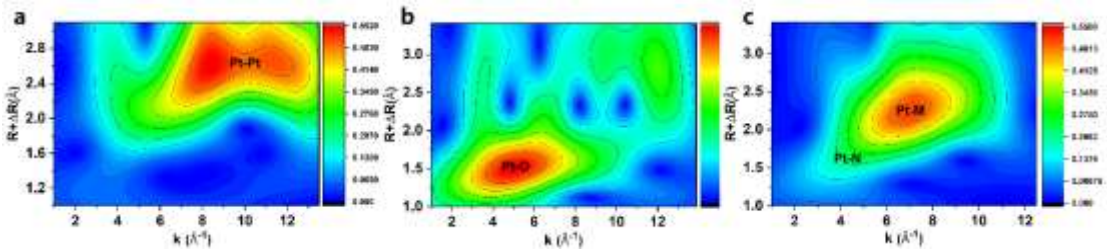

Figure S19. WT-EXAFS plots of (a) Pt foil, (b) PtO_2 and (c) PFCNCZ-HEI for Pt element.

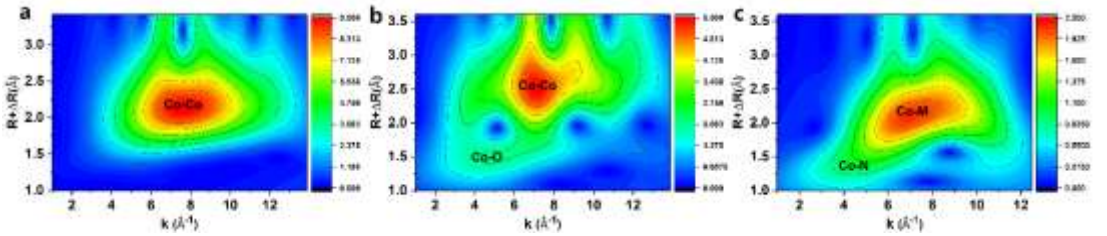

Figure S20. WT-EXAFS plots of (a) Co foil, (b) CoO and (c) PFCNCZ-HEI for Co element.

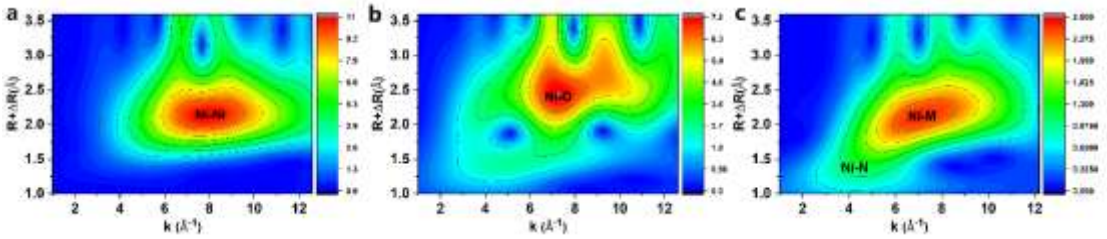

Figure S21. WT-EXAFS plots of (a) Ni foil, (b) NiO and (c) PFCNCZ-HEI for Ni element.

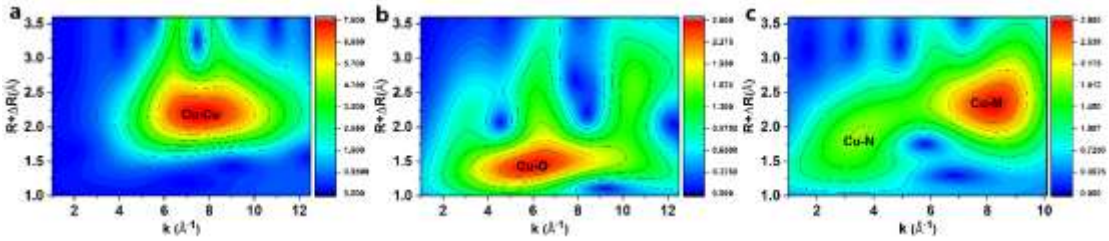

Figure S22. WT-EXAFS plots of (a) Cu foil, (b) CuO and (c) PFCNCZ-HEI for Cu element.

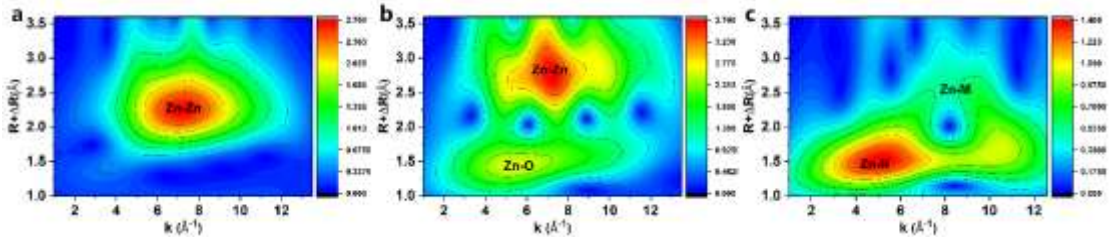

Figure S23. WT-EXAFS plots of (a) Zn foil, (b) ZnO and (c) PFCNCZ-HEI for Zn element.

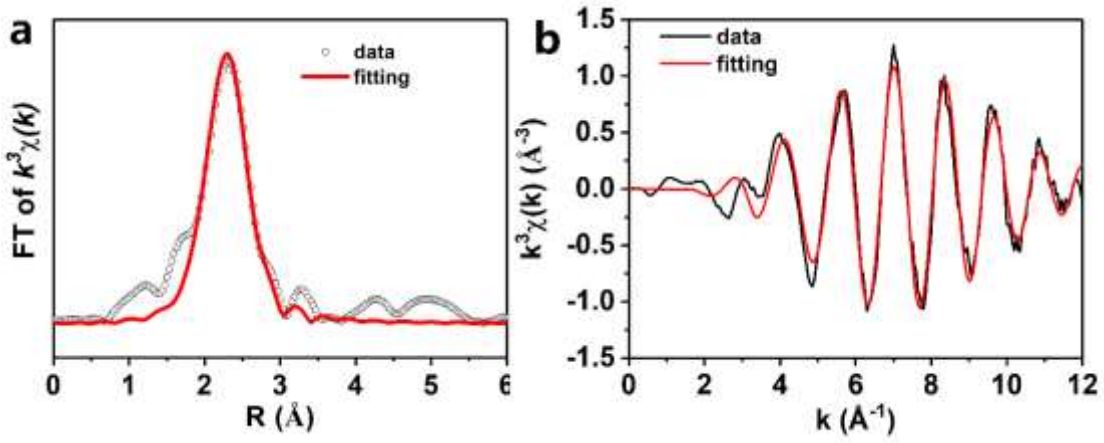

Figure S24. Comparison of the experimental k^2-weighted EXAFS and the fitting curves in the (a) R space and (b) K space for the as-prepared PFCNCZ-HEI at Pt L_3-edge.

Table S2. EXAFS fitting results for the HEA nanoparticles at Pt L_3-edge for PFCNCZ-HEI sample.

samples	path	C. N.[a]	R (Å) [b]	σ^2 ($\times$ 10^{-3} Å^2) [c]	ΔE (eV) [d]	R factor[e]
PFCNCZ-HEI	Pt-M	4.8±0.9	2.62±0.02	7.9±3.1	9.1±2.8	0.02
	Pt-Pt	3.2±0.5	2.70±0.02	5.9±3.6		

[a]C. N.: coordination numbers; [b]*R*: bond distance; [c]σ^2: Debye-Waller factors; [d]ΔE_0: the inner potential correction. [e]*R* factor: goodness of fit.

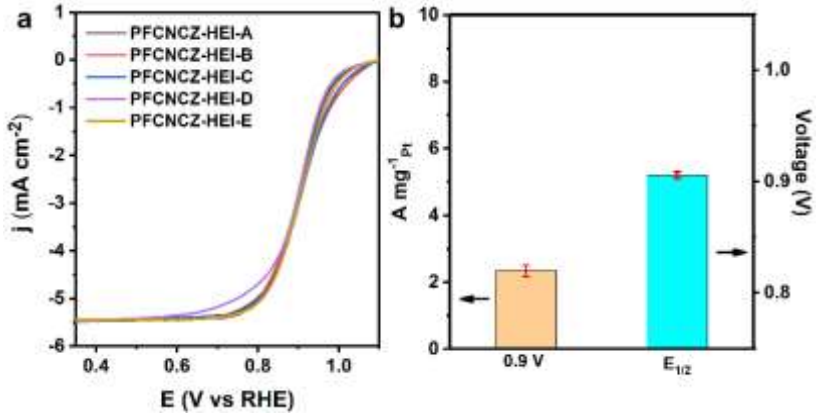

Figure S25. ORR curves of different batches of PFCNCZ-HEI samples synthesized under the same conditions. (b) Mass activities of PFCNCZ-HEI at 0.9V vs RHE and $E_{1/2}$ of PFCNCZ-HEI with error bars.

we prepared 5 batches of PFCNCZ-HEI samples, labeled as PFCNCZ-HI-A, PFCNCZ-EI-B, PFCNCZ-HEI-C, PFCNCY-HEI-D, and PFCNCZ-HTI-E. The ORR polarization curves were shown in Figure S25a. The $E_{1/2}$ values of PFCNCZ-EI-A, PFCNCZ-HEI-B, PFCNCZ-HEI-C, PFCNCY-HEI-D, and PFCNCZ-HI-E were 0.906, 0.905, 0.908, 0.901, and 0.908V, respectively, with an average value of 0.9056V and a standard deviation of 0.002881. In addition, the mass activities of PFCNCZ-EI-A, PFCNCZ-HEI-B, PFCNCZ-HEI-C, PFCNCY-HEI-D, and PFCNCZ-HI-E were 2.4, 2.233, 2.51, 2.1, and 2.44 A mg_{Pt}^{-1} at 0.9V, respectively, with an average value of

2.336 A mg_{Pt}^{-1} and a standard deviation of 0.166. The error bars were shown in Figure 25b. This indicates that different batches of PFCNCZ-HEI samples exhibit minimal fluctuations in sample performance.

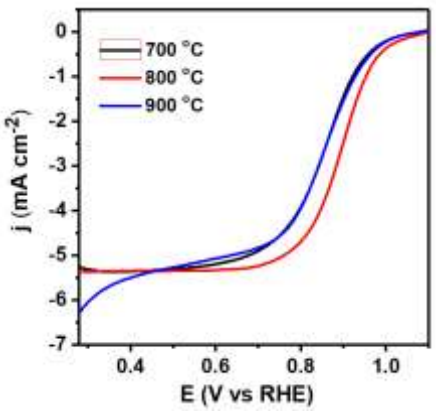

Figure S26. ORR polarization curves of PFCNCZ-HEI synthesized at different temperatures.

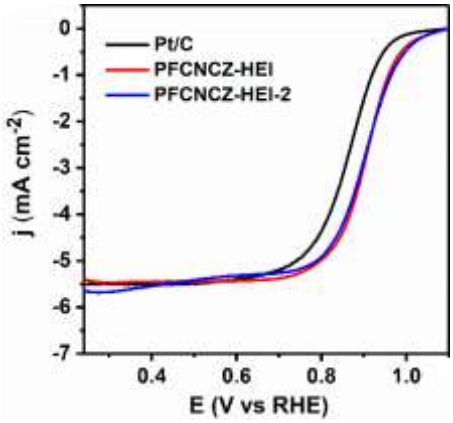

Figure S27. ORR polarization curves of Pt/C and PFCNCZ-HEI synthesized with different contents (The mass load of each element of PFCNCZ-HEI-2 sample is twice that of PFCNCZ-HEI).

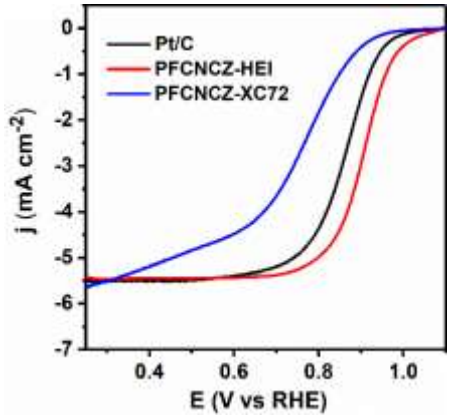

Figure S28. ORR polarization curves of Pt/C and PFCNCZ-HEI synthesized with different supports (PFCNCZ-XC72 sample is loaded on XC72).

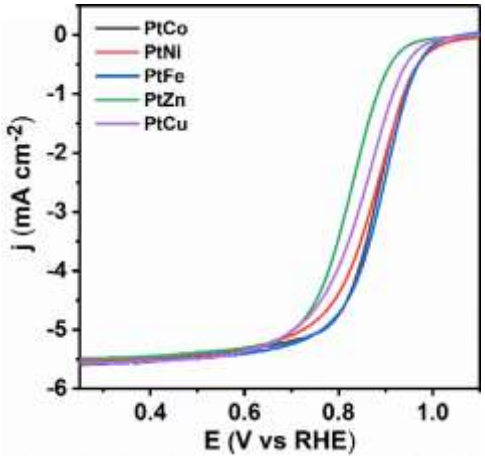

Figure S29. ORR polarization curves of the binary platinum-based intermetallic catalysts.

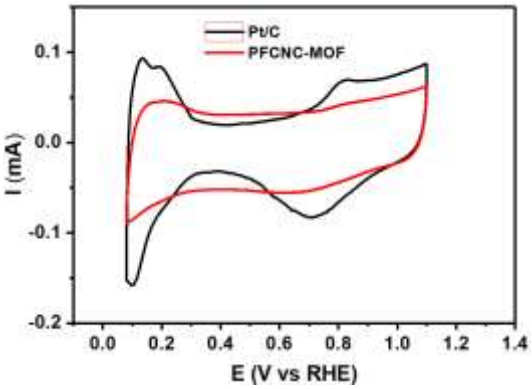

Figure S30. CV curves of the PFCNCZ-HEI and commercial Pt/C catalysts recorded in N_2-saturated 0.1 M $HClO_4$ solution at a sweep rate of 50 mV s^{-1}.

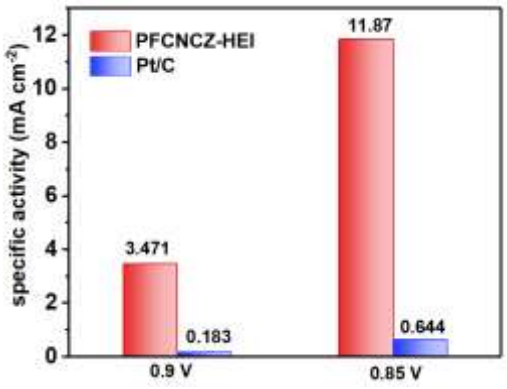

Figure S31. Specific activity of FNCNCZ-HEI and Pt/C for ORR.

Table S3. Comparison of ORR activity parameters of PFCNCZ-HEI with those of previously reported noble metal base catalysts.

catalyst	electrode	mass activity (A $mg_{noble\ metal}^{-1}$)	All-metal mass activity @ 0.9 V (A mg^{-1})	Cycle number	Decay of $E_{1/2}$ (mV)	Ref.
HEA-PtPdIrRuAg	0.1M KOH	1.69 A mg_{PGMs}^{-1}	1.69 A mg^{-1}	10000	~0mV	6
PdCuMoNiCo NPs-NHSs/RGO_3-CNT	0.1M $HClO_4$	0.882 A mg_{Pd}^{-1}	0.43 A mg^{-1}	unknown	unknown	7
AlNiCuPtPdAuCoFe	0.1M $HClO_4$	0.73 A mg_{PGMs}^{-1}	0.56 A mg^{-1}	20000	~0mV	8
PdCuPtNiCo	0.1M KOH	0.15 A mg_{PGMs}^{-1}	~0.1 A mg^{-1}	10000	8 mV	9
PtPdCoFeNi HEAs	0.1M $HClO_4$	1.17 A mg_{PGMs}^{-1}	0.7 A mg^{-1}	10000	6 mV	10
FeCoNiCuPd HEA-NPs	0.1M KOH	unknown	unknown	3000	~0mV	11
PtNiFeCuCoZn	0.1M $HClO_4$	0.5 A mg_{Pt}^{-1}	0.18 A mg^{-1}	5000	1 mV	12
Pt_3Co/C-700	0.1M $HClO_4$	0.52 A mg_{Pt}^{-1}	0.47 A mg^{-1}	5000	10 mV	13
L_{10}-FePt/Pt	0.1M $HClO_4$	0.7 A mg_{Pt}^{-1}	0.56 A mg^{-1}	5000	36 mV	14
FePt@PtBi	0.1M $HClO_4$	1.15 A mg_{Pt}^{-1}	0.88 A mg^{-1}	20000	9 mV	15
PtPd	0.1M $HClO_4$	0.89 A mg_{PGMs}^{-1}	0.89 A mg^{-1}	10000	~1mV	16
O-$Fe_3Pt/Ti_{0.5}Cr_{0.5}N$	0.1M $HClO_4$	0.673 A mg_{Pt}^{-1}	0.56 A mg^{-1}	unknown	unknown	17
PFCNCZ-HEI	0.1M $HClO_4$	2.403 A mg_{Pt}^{-1}	1.64 A mg^{-1}	10000	~0mV	This work

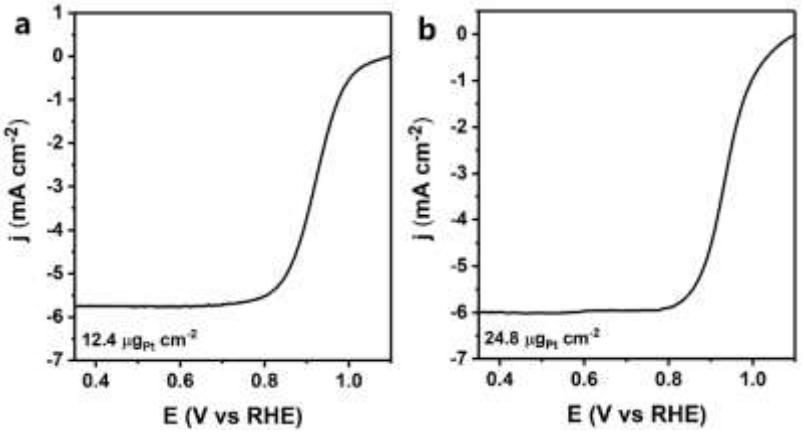

Figure S32. ORR polarization curves of FCNCZ-HEI at surface loading of (a) 12.4 μg_{Pt} cm^{-2} and (b) 24.8 μg_{Pt} cm^{-2} on RDE.

The $E_{1/2}$ of the electrodes with a Pt loading of 12.4 and 24.8 μg_{Pt} cm^{-2} reaches 0.921V and 0.937V, with corresponding mass activities of 1.81 and 1.52 A mg_{Pt}^{-1}, respectively, as shown in Figure S32. This indicates that PFCNCZ-HEI exhibits high ORR activity even at high Pt loadings. Simultaneously, it is discernible that an increase in the Pt loading leads to an overall reduction in mass activity. This phenomenon can be attributed to the fact that, for low-Pt catalysts supported on carbon, an increase in Pt loading results in a significant thickening of the carbon layer, thereby impacting mass transport. Consequently, the majority of current investigations involving low-Pt catalysts opt for conducting RDE tests under lower Pt loading conditions, allowing the intrinsic catalytic activity of the catalyst to be studied, such as Pt/Mo_2C (1.2 μg_{Pt} cm^{-2}),[18] $Pt_{1.1}$/BP (4.37 μg_{Pt} cm^{-2}),[19] Pt_3Co-*y* (2.5 μg_{Pt} cm^{-2}).[20] As a result, in the polarization curve presented in Figure 3a, the ORR polarization curves were measured under a Pt loading of 3.2 μg_{Pt} cm^{-2}.

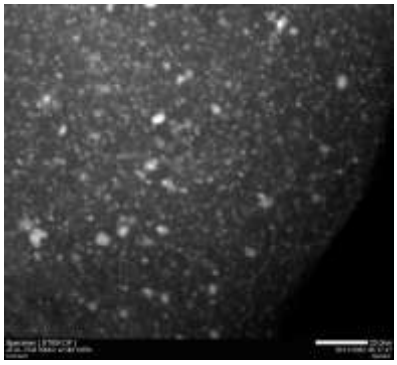

Figure S33. TEM image of PFCNCZ-HEI after 10k cycles.

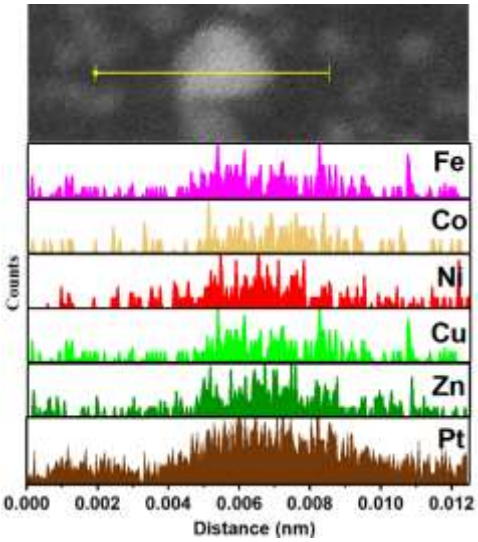

Figure S34. EDX line-scan profile of the PFCNCZ-HEI after 10k cycles.

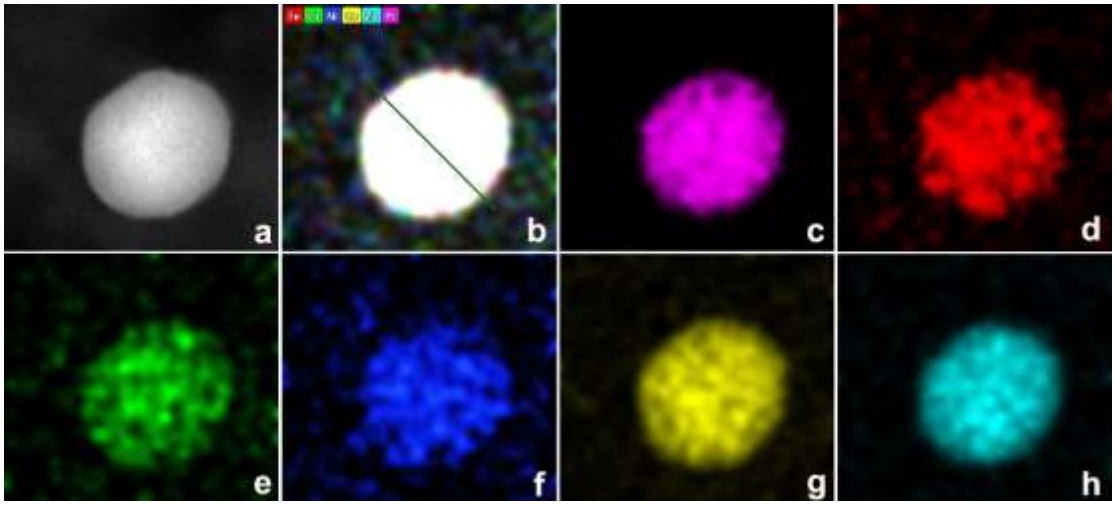

Figure S35. STEM-EDS mapping of the PFCNCZ-HEI nanoparticle after cycles. (a) Primary particle; (b) all elements; (c) Pt; (d) Fe; (e) Co; (f) Co; (g) Cu; (h) Zn.

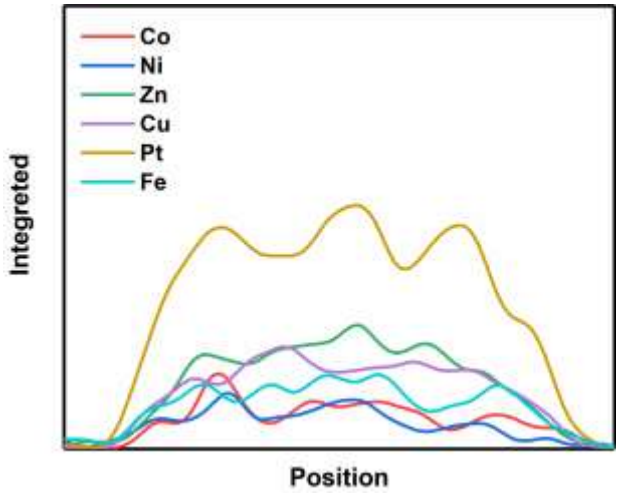

Figure S36. line-scan profile of the PFCNCZ-HEI nanoparticle along the blue line in Figure S35b after cycles.

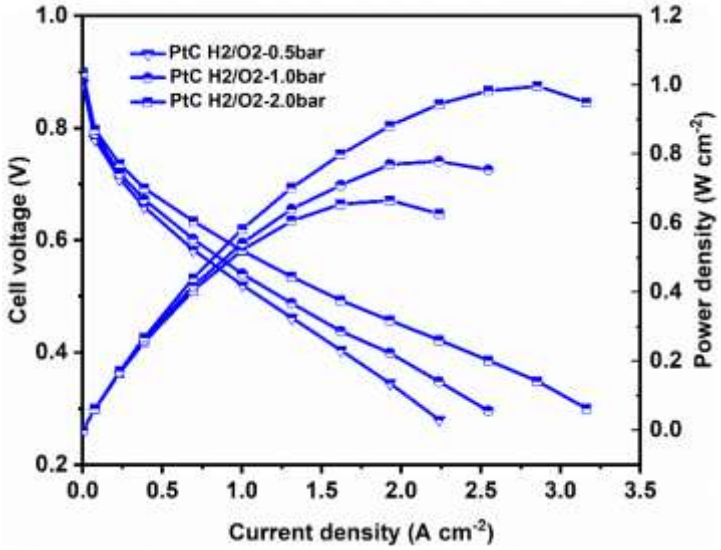

Figure S37. The I-V polarization curves and power density of H_2-O_2 fuel cell for Pt/C sample.

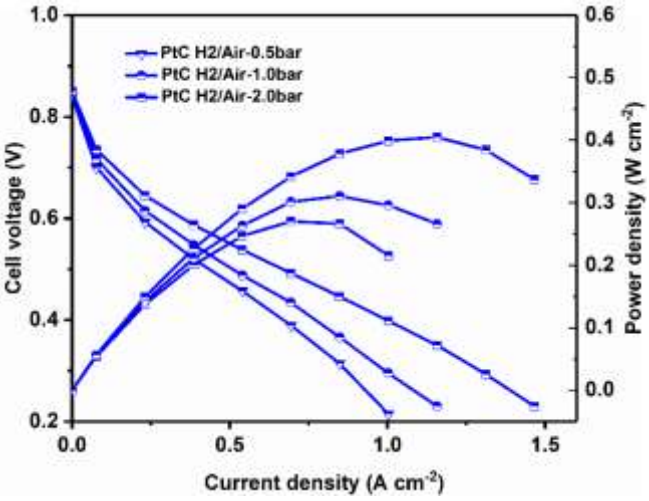

Figure S38. The I-V polarization curves and power density of H_2-Air fuel cell for Pt/C reference.

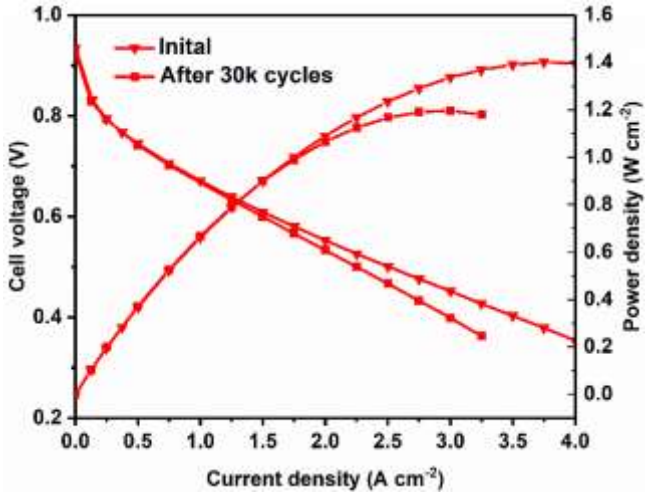

Figure S39. The I-V polarization curves and power density of H_2-O_2 fuel cell for PD-PZFCNC-HEI sample before and after ADT.

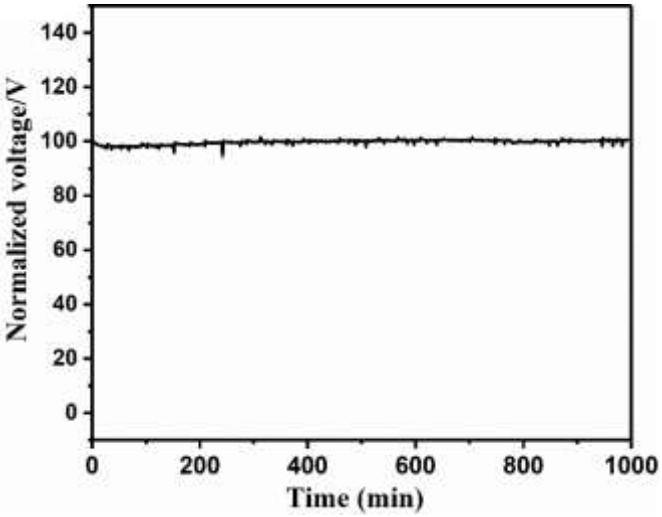

Figure S40. Long-term stability of the H_2-Air fuel cell with PFCNCZ-HEI as the cathode at a current density of 250 mA cm^{-2}.

Table S4. Comparison of key performance metrics in H_2-O_2 fuel cell for PFCNCZ-HEI versus. the state-of-the-art in the literature.

Catalysts	Load (mg_{Pt} cm^{-2})	Partial pressure (bar)	Power density (W cm^{-1})	Rated power normalized by mass (W mg_{Pt}^{-1})	reference
coplanar Pt/C NMs	0.1 mg_{Pt} cm^{-2}	2.0 bar	1.21W cm^{-2}	12.1 W mg_{Pt}^{-1}	21
PtA@FeSA-N-C	0.13 mg_{Pt} cm^{-2}	1.0 bar	1.31 W cm^{-2}	10.1 W mg_{Pt}^{-1}	22
SA-Rh/CN	0.138 mg_{Pt} cm^{-2}	1.0 bar	0.92 W cm^{-2}	6.66 W mg_{Rh}^{-1}	23
PIFCC-HEI/C	0.1 mg_{Pt} cm^{-2}	2.0 bar	1.8 W cm^{-2}	18 W mg_{Rh}^{-1}	24
sub-Pt_3Co-MC	0.2 mg_{Pt} cm^{-2}	1.5 bar	1.77 W cm^{-2}	8.85 W mg_{Pt}^{-1}	25
Pt_1–Fe/Fe_2O_3	0.009 mg_{Pt} cm^{-2}	unknown	0.24 W cm^{-2}	27 W mg_{Pt}^{-1}	26
Cu-PtFe/NC	0.5 mg_{Pt} cm^{-2}	unknown	0.882 W cm^{-2}	1.7 W mg_{Pt}^{-1}	27
PtCo@Gnp	0.076 mg_{Pt} cm^{-2}	1.5 bar	1.01 W cm^{-2}	13.2 W mg_{Pt}^{-1}	28
$Pt_{78}Zn_{22}$/KB	0.15 mg_{Pt} cm^{-2}	1.5 bar	1.4 W cm^{-2}	9.33 W mg_{Pt}^{-1}	29
$Pt_{61}Te_8Rh_{31}$ NRs/C	0.3 mg_{Pt} cm^{-2}	1.5 bar	1.85 W cm^{-2}	6.16 W mg_{Pt}^{-1}	30
PtNi-BNCs	0.15 mg_{Pt} cm^{-2}	3.0 bar	0.92 W cm^{-2}	6.13 W mg_{Pt}^{-1}	31
PtNiCo/NC	0.114 mg_{Pt} cm^{-2}	1.5 bar	1.074 W cm^{-2}	9 W mg_{Pt}^{-1}	32
L10-PtZn	0.16 mg_{Pt} cm^{-2}	1.5 bar	2.0 W cm^{-2}	12.5 W mg_{Pt}^{-1}	33
Pt_3Co/DMC-F	0.2 mg_{Pt} cm^{-2}	3.0 bar	0.85 W cm^{-2}	4.25 W mg_{Pt}^{-1}	34
Au-PtCo/C	0.2 mg_{Pt} cm^{-2}	1.6 bar	1.12 W cm^{-2}	5.6 W mg_{Pt}^{-1}	35
PFCNCZ-HEI	0.03 mg_{Pt} cm^{-2}	2.0 bar	1.24 W cm^{-2}	45 W mg_{Pt}^{-1}	This work

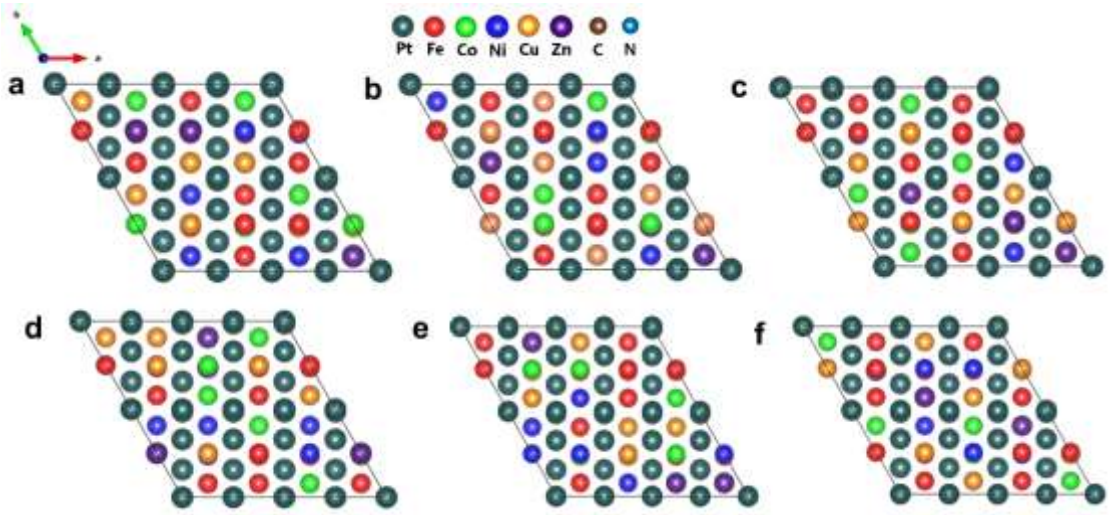

Figure S41. (a-f) Constructed a series of PFCNZ-HEI (111) surface models.

Considering that the space group of PFCNCZ-HEI is P4/mm (JCPDS PDF#43-1359), as shown in Figure 1c, a series of theoretical calculation models by randomly distributed different light transition metal atoms in M metal sites on the (111) plane was constructed based on the different atomic ratios in the PFCNCZ-HEI formula. Subsequently, the models were optimized, and final six surface models (corresponding to Figure 41a-f) were selected, each demonstrating stable energy convergence. The surface formation energies for Figure 41a-f are -674.9, 674.2, -674.9, -674.6, -673.7, and -675.9 eV, respectively. Among them, the structure in Figure S41a shows the lowest surface energy, and all six different atoms are present on the outermost layer, which is favorable for

the subsequent theoretical exploration of the activity contribution of each metal element. Therefore, the model from Figure 41a was determined as the final computational model.

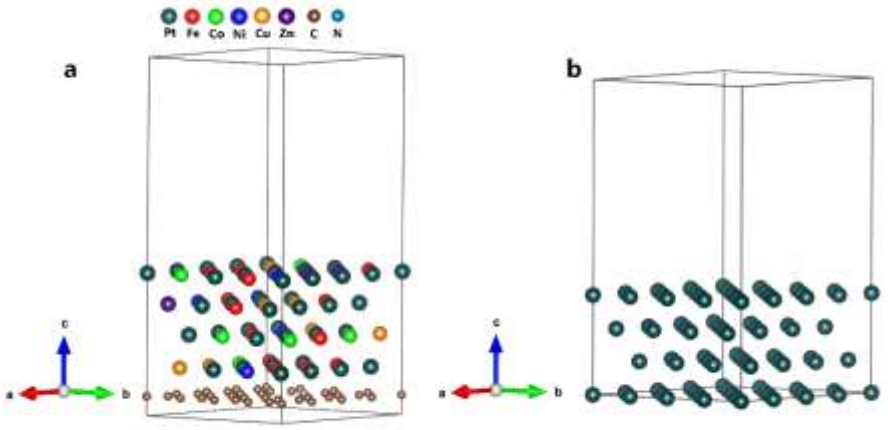

Figure S42. (a) PFCNCZ-HEI model and (n) Pt for DFT calculated. (red:Fe;)

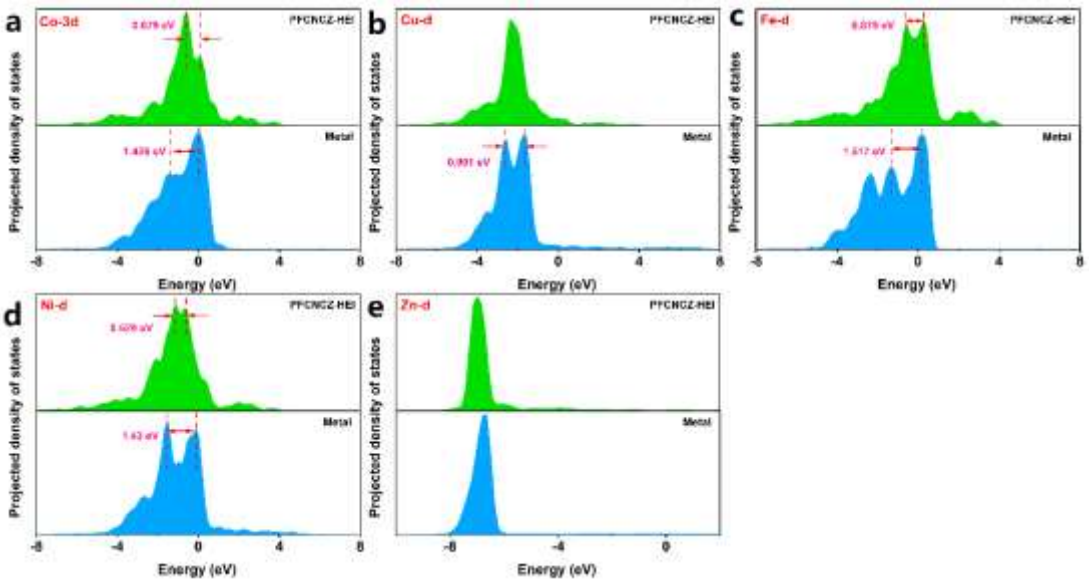

Figure S43. PDOS of (a) Co-d, (b) Cu-d, (c) Fe-d, (d), Ni-d, (e) Zn-d and corresponding pure metal.

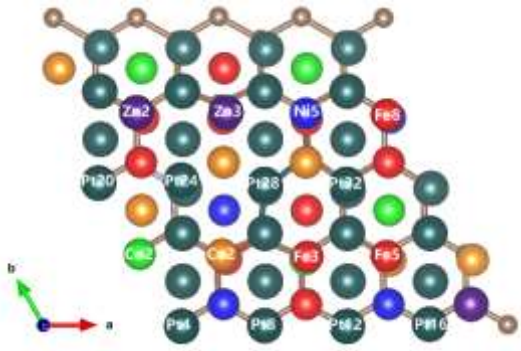

Figure S44. PFCNCZ-HEI model and its labeling of surface sites.

Table S5. GO - GOH values of each site on the upper surface of PFCNCZ-HEI model.

Element site	d-band center (eV)	GO (eV)	GOH (eV)	GO-GOH (eV)
Co2	-0.847	1.03466	0.41723	0.617
Ni5	-1.225	1.17892	0.68476	0.494
Fe3	-0.77	0.95794	0.33381	0.624
Fe5	-0.789	-0.1282	0.42887	-0.557
Fe8	-0.739	0.82681	0.27051	0.556
Cu2	-2.256	0.5292	0.44434	0.008
Zn2	-6.601	1.11104	0.31843	0.793
Zn3	-6.657	1.11367	0.32444	0.789
Pt4	-2.665	0.78258	0.45192	0.331
Pt8	-2.767	0.79722	1.0913	-0.294
Pt12	-2.848	1.25288	1.25893	-0.006
Pt16	-2.736	1.56209	0.12933	1.432
Pt20	-2.896	0.70048	0.8996	-0.199
Pt24	-2.59	1.11159	0.33175	0.780
Pt28	-2.566	1.17968	0.79946	0.380
Pt32	-2.8	0.35323	0.3191	0.034

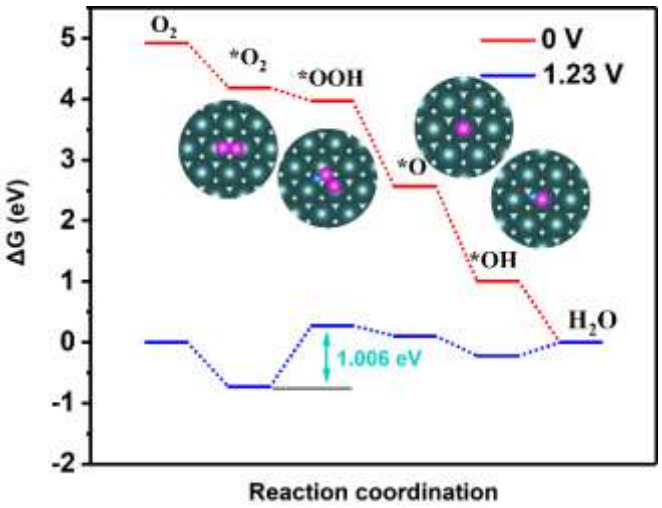

Figure S45. The free energies of intermediates on Pt (111) for the ORR steps.

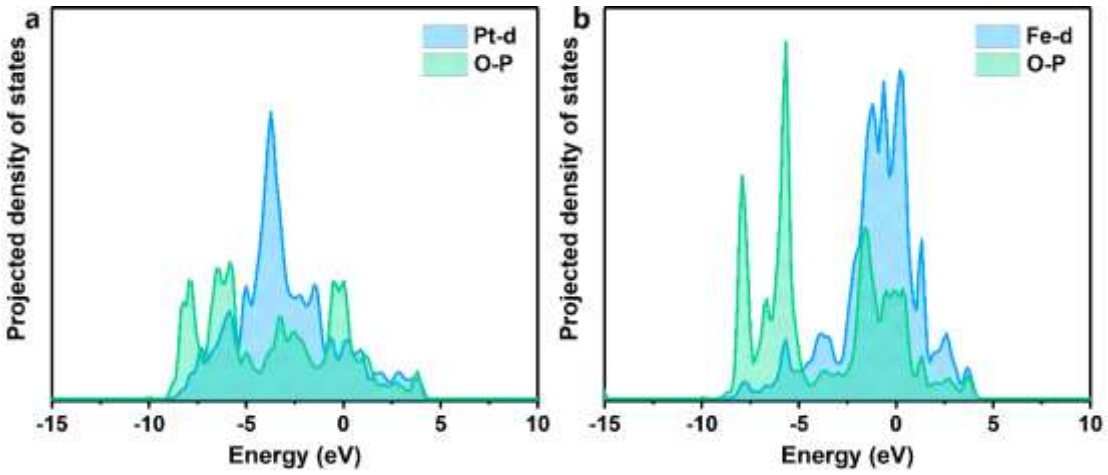

Figure S46. (a) PDOS of Pt-d and O-p for Zn28 sites at $*O_2$ state. (b) PDOS of Fe-d and O-p for Fe8 sites at $*O_2$ state

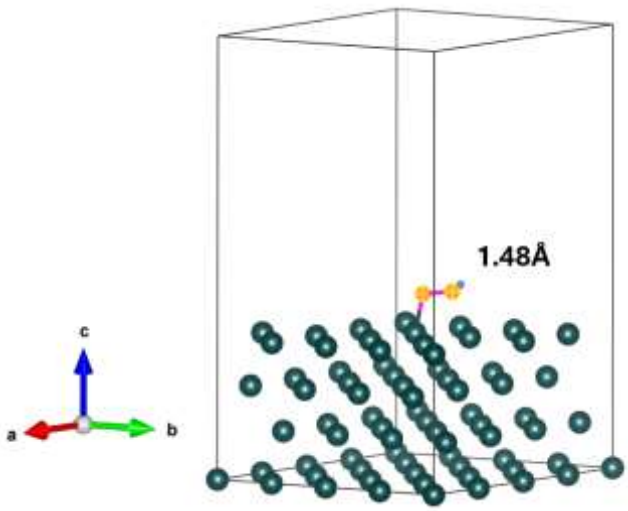

Figure S47. O-O bond length of *OOH at Pt (111).

References.

[1] G. Kresse and J. Furthmüller, Phys. Rev. B, 1996, 54, 11169–11186.

[2] P. E. Blöchl, Phys. Rev. B, 1994, 50, 17953–17979.

[3] Phys. Rev. Lett., 1996, 77, 3865–3868.

[4] The Journal of Chemical Physics, 2010, 132, 154104.

[5] J. Phys. Chem. B, 2004, 108, 17886–17892.

[6]. J. Am. Chem. Soc. 2022, 144, 10582−10590.

[7]. J. Mater. Chem. A, 2022, 10, 14857–14865.

[8]. J. Mater. Chem. A, 2019, 7, 6499–6506.

[9]. ACS Nano 2022, 16, 18873−18885.

[10]. Nano research 2022, 15, 7868-7876.

[11]. Chem. Commun., 2021, 57, 2637-2640.

[12]. Adv. Funct. Mater. 2022, 32, 2204110.

[13]. Nat. Mater. 2013, 12, 81-87.

[14]. J. Am. Chem. Soc. 2018, 140, 2926-2932.

[15]. ACS Catal. 2021, 11, 184−192.

[16]. J. Am. Chem. Soc. 2021, 143, 496−503.

[17]. Adv. Energy Mater. 2018, 1803040.

[18] Adv. Sci. 2021, 8, 2101344.

[19] Angew.Chem.Int.Ed.2019,58,1163.

[20] ACS Energy Lett. 2023, 8, 628.

[21]. Angew. Chem. Int. Ed. 2021, 60, 6533 – 6538.

[22]. Energy Environ. Sci., 2020, 13, 3032—3040.

[23]. Tian et al., Science 2019, 366, 850–856.

[24]. J. Am. Chem. Soc. 2023, 145, 11140-11150.

[25]. PNAS 2021,118, ,35.

[26]. Nature energy, 2021, 6, 614–623.

[27]. Adv. Funct. Mater. 2022, 32, 2109244.

[28]. nature nanotechnology, 2022, 17, 968–975.

[29]. Adv. Sci. 2022, 9, 2200147.

[30]. Energy Environ. Sci., 2022, 15, 3877–3890

[31]. Tian et al., Science 2019, 366, 850–856.

[32]. Applied Catalysis B: Environmental 2019, 258, 117947.

[33]. Adv. Energy Mater. 2020, 10, 2000179

[34]. J. Mater. Chem. A, 2020, 8, 15822–15828

[35]. Applied Catalysis B: Environmental 2019, 247, 142–149.